Check for updates

Electrostrain optimization of $Bi_{0.5}Na_{0.5}TiO_3$-based lead-free piezoceramics by $CaZrO_3$ modifying

Haipeng Zhu[1], Jinyuan Wu[1], Fayaz Hussain[2], Tao Ni[1], Jiajing Li[1], Yan Wang[1], Hao Xi[3], Minmin Mao[1],*, Ji Hu[1], Bing Liu[1], and Kaixin Song[1],*

[1] College of Electronics and Information, Hangzhou Dianzi University, Hangzhou 310018, China
[2] Department of Materials Engineering, NED University of Engineering and Technology, Karachi 75270, Pakistan
[3] LG Energy Solution Technology (Nanjing), Co., Ltd, Nanjing 210046, China

ABSTRACT

$Bi_{0.5}Na_{0.5}TiO_3$ (BNT)-based ceramics with excellent electrostrain properties are considered to be one of the most promising lead-free alternative systems. In this work, appropriately deviating from the morphotropic phase boundary (MPB) range, the ceramics of $(1-x)(0.75Bi_{0.5}Na_{0.5}TiO_3$-$0.25Bi_{0.5}K_{0.5}TiO_3)$-$xCaZrO_3$ (abbreviated as 0.75BNT-0.25BKT-xCZ, x = 0, 0.01, 0.03, 0.05) were synthesized by the solid-state reaction method. The phase structure combined with the dielectric, ferroelectric, and field-induced strain properties was systematically analyzed. The X-ray diffraction patterns showed that CZ was well incorporated into the 0.75BNT-0.25BKT structure to form a single-solid solution. As CZ content increases, the phase structure constructed by the coexistence of rhombohedral and tetragonal phases gradually transforms into the pseudocubic phase. Meanwhile, the dielectric temperature spectra demonstrated the coexistence of ferroelectric and relaxor phases during the phase transition with the formation of the weakly coupled relaxor, implying the presence of nanodomains which were further confirmed by the high-resolution transmission electron microscopy image. Interestingly, the maximum unipolar strain of 0.34% with a prominent increase of 70% and the hysteresis of 33% with a moderate increase of 26% were obtained simultaneously at x = 0.03 as compared to those at x = 0 (0.75BNT-0.25BKT). Further to this, this study investigated the origin of the large strain together with hysteresis variation and considered that reversible phase transition combined with relaxation behavior helps realize a tradeoff between large strain and low hysteresis, which provides an effective path for the further development of high-performance lead-free piezoelectric ceramics.

Address correspondence to E-mail: mmm@hdu.edu.cn; kxsong@hdu.edu.cn

Springer

1 Introduction

Piezoelectric ceramics with electrostrain properties can be utilized to realize micro-displacement with high resolution and fast response, which are frequently employed in laser frequency stabilization, probe shifting, optical scanning, etc. [1–3]. However, with device miniaturization and precision improvement, micro-displacement should get higher resolution, better linearity, and reliability, which requires piezoelectric ceramics with larger electrostrain and lower nonlinear hysteresis [4, 5]. In addition, the trend of green products for environmental protection requires the development of lead-free electronic ceramics [6, 7]. Due to their outstanding electrostrain properties, the $Bi_{0.5}Na_{0.5}TiO_3$ (BNT)-based piezoelectric ceramics are considered to be one of the most promising lead-free alternatives and have been extensively explored so far. For example, Wu et al. attained an ultrahigh strain of 0.74% with a d_{33}^* of 1057 pm/V in the $Sr_x(Bi_{1-x}Na_{0.97-x}Li_{0.03})_{0.5}TiO_3$ system, demonstrating the enormous potential of BNT-based ceramics [8].

Several optimization strategies for the electrostrain performance of BNT-based ceramics have been reported, among which, chemical modification to construct multi-component solid solutions is an effective method [1, 9, 10]. For a solid solution, the selection of base composition is important. Generally, $Bi_{0.5}Na_{0.5}TiO_3$-$xBaTiO_3$ (BNT-BT, $x = 0.06–0.1$) and $Bi_{0.5}Na_{0.5}TiO_3$-$xBi_{0.5}K_{0.5}TiO_3$ (BNT-BKT, $x = 0.16–0.22$) in the morphotropic phase boundary (MPB) range are widely used as base compositions due to their excellent piezoelectricity [10, 11]. For instance, Zhang et al. constructed MPB between rhombohedral and tetragonal phases in BNT-BT and introduced $K_{0.5}Na_{0.5}NbO_3$ (KNN) to construct ternary solid solutions, yielding a giant strain of 0.45% [12]. Similarly, Hao et al. acquired a giant strain of 0.46% in the $(1-x)(0.8BNT-0.2BKT)$-$xKNN$ system [13]. Liu et al. also obtained a large strain of 0.33% in $0.99Bi_x(Na_{0.8}K_{0.2})_{0.5}TiO_3$-$0.01SrTiO_3$ [14]. Unfortunately, a large strain is usually accompanied by serious hysteresis [2, 4, 15]. The larger hysteresis it has, the lower precision of micro-displacement will be [1, 3]. In the above studies, the hysteresis values of about 48.8%, 65%, and 61.5% were obtained, respectively, which could not match the demands of high-precision micro-displacement.

However, it is possible to obtain reduced hysteresis with maintained relatively large strain by deviating the base composition from the MPB range appropriately. For example, near the MPB, Qian et al. created $0.96(0.75BNT–0.25BKT)$-$0.04BiAlO_3$ with a moderate strain of 0.21% and a low hysteresis of 24%, proving their hypothesis that hysteresis can be lowered by blurring the phase boundary of the ferroelectric relaxor phase via the coexistence of numerous polar nanodomains [16]. Furthermore, Liu et al. attained an ultralow hysteresis of 4.7% with a strain of 0.18% in the $(1-x)(0.75BNT-0.25BKT)$-$xSrTiO_3$ system [4]. On the other hand, studies show that the reversible phase transition from the relaxor phase to the ferroelectric phase induced by the electric field is the main source of large strain in BNT-based ceramics with multiphase coexistence. Han et al. achieved the coexistence of ferroelectric and relaxor phases by incorporating Ta_2O_5 into the $Bi_{0.5}(Na_{0.72}K_{0.22}Li_{0.06})_{0.5}TiO_3$, which exhibited a pinched hysteresis loop and obtained a large strain of 0.385% contributed by the reversible phase transition [17]. According to the aforesaid phenomena, appropriately deviating from MPB and incorporating a relaxor phase to establish multiphase coexistence combined with the reversible phase transition and high dynamic polar-nanoregions (PNRs), the tradeoff between large strain and low hysteresis has the promise to be realized.

As per the above idea, i.e., near the MPB, we formulated the $(1-x)(0.75Bi_{0.5}Na_{0.5}TiO_3$-$0.25Bi_{0.5}K_{0.5}TiO_3)$-$xCaZrO_3$ ($0.75BNT$-$0.25BKT$-xCZ) ceramic system, where $CaZrO_3$ (CZ) is a non-ferroelectric with a perovskite structure. In this case, the introduction of CZ could not only disrupt the long-range ferroelectric order but also induce site disorder and charge fluctuation, which would be helpful to realize the coexistence of ferroelectric and relaxor phases with associated PNRs [18]. Based on this, a balance between the large strain and low hysteresis could be obtained through the reversible phase transition from the relaxor phase to the ferroelectric phase and the high dynamic PNRs. We systematically investigated the dielectric, ferroelectric, and electrostrain properties and discussed the origin of electrostrain based on the structure–property relationship analysis. This work advances our understanding of the electrostrain mechanism and provides an effective approach to comprehensively optimizing the electrostrain properties of BNT-based ceramics.

2 Experimental procedure

$(1–x)(0.75Bi_{0.5}Na_{0.5}TiO_3-0.25Bi_{0.5}K_{0.5}TiO_3)-xCaZrO_3$ (0.75BNT-0.25BKT-xCZ, x = 0, 0.01, 0.03, 0.05) ceramics were synthesized by a standard solid-state reaction method. High-purity oxides and carbonates (> 99.9%, all from Aladdin) of Bi_2O_3, TiO_2, $CaCO_3$, ZrO_2, Na_2CO_3, and K_2CO_3 were used as raw materials. All raw materials were dried before use, subsequently weighed according to stoichiometric formulae, and ball milled in ethanol for 24 h. The dried slurry was calcined in an alumina crucible at 875 °C for 3 h and then similarly ball milled again. The dried powder was mixed with 5wt% polyvinyl alcohol and pressed into green disks with a diameter of 13 mm and a thickness of 1.2 mm. After the binder was burned at 600 °C, the pellets were immediately sintered at 1100 °C for 3 h at a heating rate of 5 °C/min followed by cooling to 850 °C at a rate of 3 °C/min and finally to room temperature (RT) naturally. During this process, the green disks were already buried in sacrificing powders of the same composition to avoid the volatility of Bi, Na, and K. The relative density of all samples was measured using the Archimedes method.

The crystal structures of the ceramics were analyzed by X-ray diffraction (XRD, Smartlab 3 kW, Rigaku, Japan) using Cu Kα radiation (λ = 1.5406 Å) in the 2θ range of 10–80° at a step of 0.02° at RT. The surface morphology of the ceramics was identified by scanning electron microscopy (SEM, JSM-6510, JEOL Ltd., Tokyo, Japan). The high-resolution transmission electron microscopy (HRTEM) images were obtained by a FEI Tecnai F30 operated at 300 kV, while the Fast Fourier transformation (FFT) and Inverse Fast Fourier transformation (IFFT) were conducted using Digital Micrograph software (Gatan, Pleasanton, CA, USA). To characterize the electrical properties, the sintered samples were polished down to a thickness of around 0.5 mm and both sides were covered by silver electrodes with a diameter of 6 mm. The dielectric properties were measured using a precision impedance analyzer (HP4294A, Hewlett Packard Co., Palo Alto, CA) from 35 to 400 $^\circ$C with a heating rate of 2 $^\circ$C/min at different frequencies from 1 kHz to 1 MHz. The polarization versus electric field loops (P–E) and electric field-induced strain (S–E) curves were measured in a silicone oil bath at RT using a ferroelectric analyzer (Precision Premier II, Radiant Technology, USA). The piezoelectric coefficient (d_{33}) was tested on poled samples using a quasi-static piezo-d_{33} tester (ZJ–3AN, Chinese Academic Society, China).

3 Results and discussion

The X-ray diffraction patterns in Fig. 1a show that all samples exhibit a pure perovskite structure without any observable secondary phase within the accuracy. It indicates that CZ is well incorporated into 0.75BNT-0.25BKT to form a solid solution. Figure 1b exhibits the enlarged patterns for the 2θ range of 38°–42° and 45°–48°. For x = 0, the trace of typical splitting peaks $(111)_R$ and $(002)_T$ for the rhombohedral and tetragonal phases is observed near 39.5° and 46°, respectively, which reveals the coexistence of the tetragonal and rhombohedral phases [8, 19]. As x increases, the trace of splitting gradually disappears to leave a single recognizable peak, implying that the phase structure gradually transforms from the coexistence of rhombohedral and tetragonal phases to the pseudocubic phase. Meanwhile, the (200) peak gradually shifts to the lower angle, while the location of the (111) peak is essentially unaltered. According to Bragg's law and the other reported works, the former indicates the increase of lattice constant a and the latter implies the decrease of the lattice constant c [15, 20]. The above phenomena could be ascribed to the dual contribution of A- and B-site co-substitution, in which the substitution of Zr^{4+} (0.72Å) for Ti^{4+} (0.605Å) should cause an expansion in the size of the B-site, while the substitution of Ca^{2+} (1.34Å) for A-site ions, including Bi^{3+} (1.36Å), Na^+ (1.39Å), and K^+ (1.64Å), should cause a shrink in the size of the A-site [19]. Ultimately, the effect of ion substitution on the lattice is manifested in the variation of the diffraction peaks.

Figure 2 displays the surface morphology of 0.75BNT-0.25BKT-xCZ ceramics. It is discovered that all the samples are dense with square-shaped grains (above 95% relative density, see Fig. S1). There are no substantial changes in average grain size when x = 0–0.03 with the remained value of about 0.65 μm. As x increases to 0.05, the average grain size increases rapidly to 0.84 μm as well as the standard deviation of grain size. The variation of average grain size and standard deviation is also shown in Fig. S1. It should be attributed to the extensive CZ doping, causing certain local defects with site disorder which

Fig. 1 X-ray diffraction patterns of 0.75BNT-0.25BKT-xCZ (x = 0 –0.05) ceramics in the range of 2θ: **a** 10°–80°; **b** 38°–42°; and 45°–48°. Subscripts pc, R, and T refer to pseudocubic, rhombohedral, and tetragonal structures, respectively
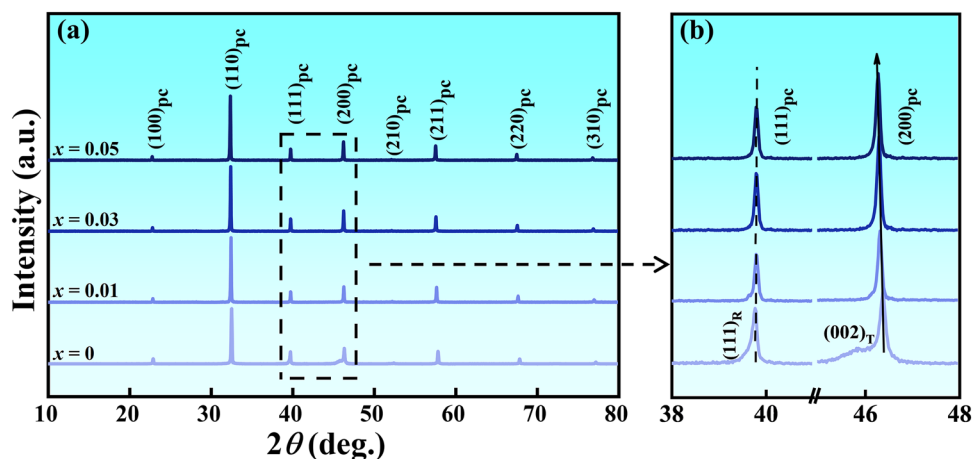
Fig. 2 SEM images of surface morphology for as-sintered 0.75BNT-0.25BKT-xCZ samples: **a** x = 0, **b** x = 0.01, **c** x = 0.03, and **d** x = 0.05
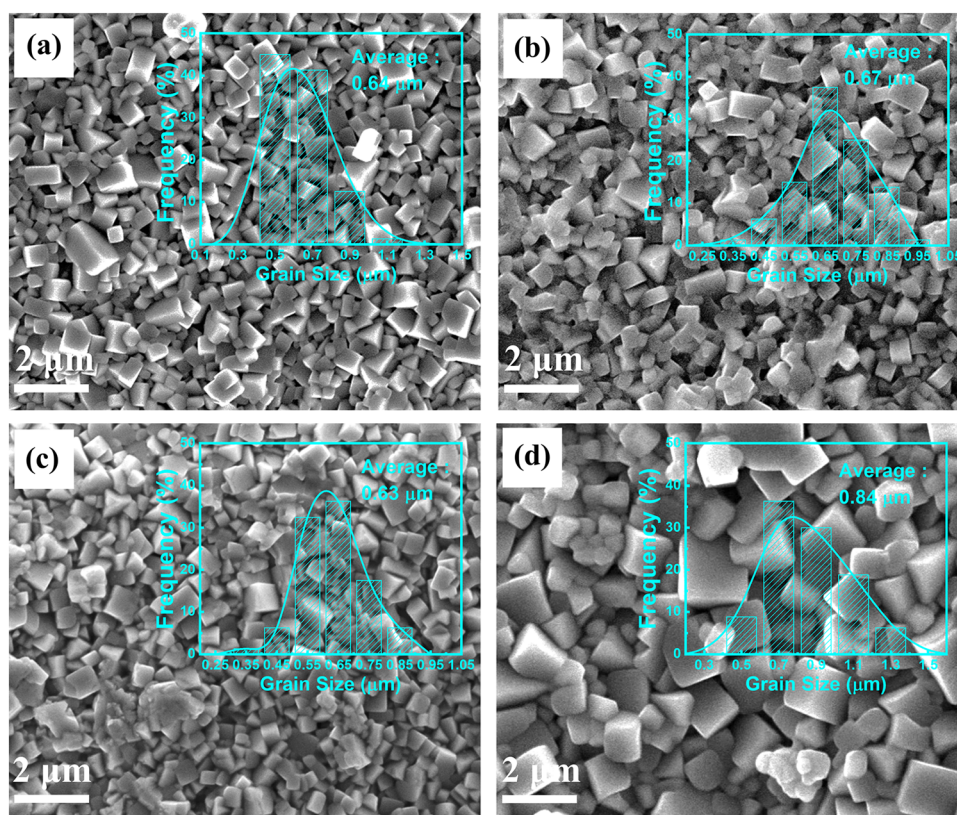

enhances grain boundary migration and thus abnormal grain growth [21].

Figure 3a shows the dielectric temperature spectrum of the 0.75BNT-0.25BKT-xCZ ceramics at 1 kHz –1 MHz. Two distinctive dielectric anomalies are observed within the measured range, denoted as T_s and T_m, respectively, which are usually reported in BNT-based ceramics [22–24]. The former anomaly T_s located at the low-temperature shoulder is considered to be generated by the thermal activation of

PNRs for $R3c$ and $P4bm$ [11, 25]. The latter one T_m corresponding to the maximum relative permittivity is thought to be contributed by the transition from $R3c$ to $P4bm$ and the thermal evolution of PNRs for $P4bm$ [26, 27]. On the other hand, the broadened peaks of T_s shift to the higher temperature as well as the corresponding peaks of dielectric loss with increasing frequency, while the broadened peaks of T_m are insensitive to frequency change. The above phenomena of typical features with frequency

Fig. 3 a Temperature dependence of relative permittivity and dielectric loss of 0.75BNT-0.25BKT-xCZ samples at different frequencies. **b** The variation of relative permittivity and dielectric loss with varying x at 1 kHz. **c** Plot of ln (1/ε−1/ε_m) versus ln (T−T_m) based on the Curie–Weiss law at 1 kHz. **d** The temperature dependence of reciprocal of relative permittivity for x = 0.03. Plots of Vogel–Fulcher fitting for **e** x = 0 and **f** x = 0.03
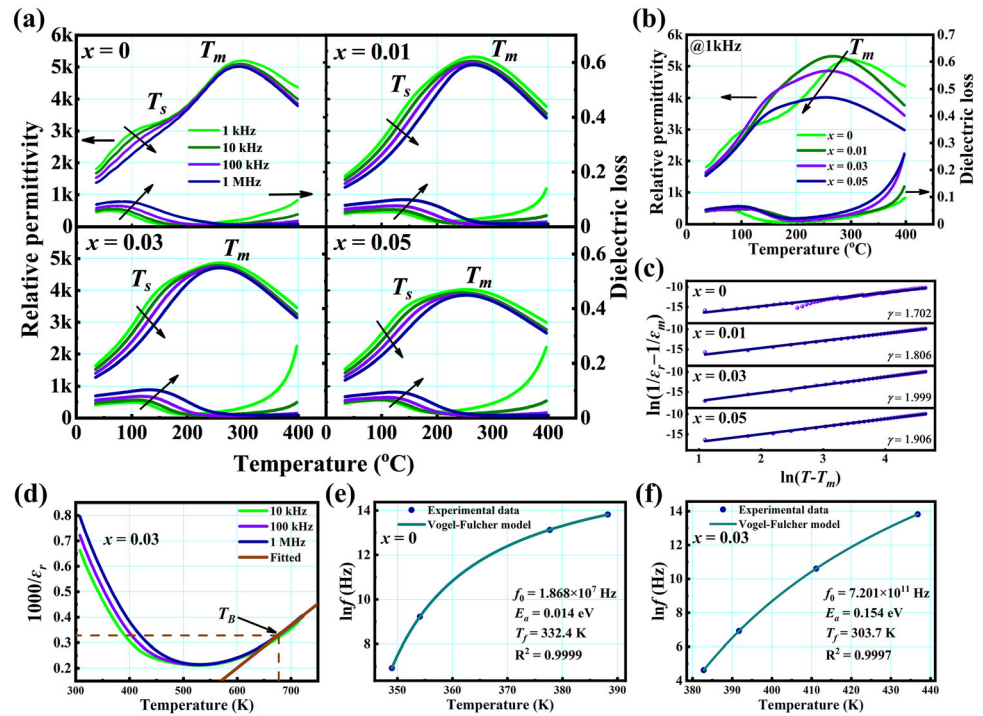
dispersion and diffused phase transitions indicate the obvious relaxation characteristics for the ceramics [28, 29]. Moreover, the temperature dependence of relative permittivity and dielectric loss with various x at 1 kHz is shown in Fig. 3b. It can be found that the relative permittivity gradually decreases and T_m shifts toward lower temperatures as the doping level increases, which may be attributed to site disorder and charge fluctuation, resulting in enhanced relaxation [30, 31].

In order to evaluate the relaxation behaviors of the 0.75BNT-0.25BKT-xCZ ceramics, the modified Curie–Weiss formula is adopted as follows [32]:

$$\frac{1}{\varepsilon_r} - \frac{1}{\varepsilon_m} = \frac{(T - T_m)^\gamma}{C},$$ (1)

where ε_r is the relative permittivity, ε_m is the maximum of the relative permittivity, C is the Curie constant, and γ is usually used to quantify the system's degree of relaxation ($1 \leq \gamma \leq 2$). It is usually regarded that the system is in a normal ferroelectric state as $\gamma = 1$, while in an ideal relaxor ferroelectric state as $\gamma = 2$ [14]. The value of γ is calculated according to Eq. (1) and the fitted results are shown in Fig. 3c. It is observed that the value of γ increases from 1.702 at x = 0 to 1.999 at x = 0.03, indicating that the addition of CZ enhances the relaxation degree. As x further increases to 0.05, the value of γ slightly drops to 1.906,

which may be related to the defects of the microstructure due to irregular grain growth mentioned in Fig. 2. In addition, to further explore the stability of the relaxor phase, the Burns temperature (T_B) referred to the transition temperature from the relaxor phase to the paraelectric phase can be obtained by estimating the deviation from Curie–Weiss law upon the reciprocal of relative permittivity [18]. In Fig. 3d, T_B is estimated to be over 675 K for x = 0.03, indicating the high thermal stability of the relaxor phase.

Furthermore, the Vogel–Fulcher formula is used to better comprehend the origin of relaxation behavior, given as follows [33]:

$$f = f_0 \exp\left(-\frac{E_a}{K_B (T_p - T_f)}\right),$$ (2)

where f and f_0 are the operating frequency and Debye frequency, respectively, K_B is the Boltzmann constant, and T_p is the temperature at which the maximum imaginary part of the dielectric constant is attained. E_a is the relaxation activation energy that represents the polarization oscillation barriers between adjoining PNRs. T_f is the dipole freezing temperature, defining the transition temperature from the non-ergodic relaxor to the ergodic relaxor [34, 35]. If the operating temperature falls below T_f,

samples will be in the non-ergodic relaxor state, which means the reorientation of PNRs will be difficult after removing the external excitation. Instead, samples will be in the ergodic state, and PNRs will be activated with high dynamic when the operating temperature surpasses T_f [36]. In addition, it is important to emphasize that the T_f obtained from the Vogel–Fulcher formula is merely a statistical value, not all PNRs are activated above T_f, and vice versa [34]. The fitted results with high correlation coefficients ($R^2 > 0.999$) for $x = 0$ and $x = 0.03$ are exhibited in Fig. 3e and f. When x increases from 0 to 0.03, T_f decreases from 332.4 K to 303.7 K, which is close to RT, indicating the enhanced dynamics of PNRs and the possibility of coexistence of the ergodic relaxor and ferroelectric phases at RT. On the other hand, E_a increases substantially from 0.014 eV ($x = 0$) to 0.154 eV ($x = 0.03$). Herein, high E_a implies the formation of the weakly coupled relaxor, in which the interaction force between adjacent PNRs is relatively weak and the polar clusters are isolated and frustrated [37]. Consequently, achieving a long-range dipole alignment is difficult even in the presence of a strong electric field [35]. These results illustrate the high dynamic of PNRs at $x = 0.03$ and further demonstrate the effectiveness of CZ introduction to enhance relaxation behavior significantly.

In order to further probe the structural details to prove the existence of PNRs, HRTEM imaging was conducted on the 0.75BNT-0.25BKT-0.03CZ ceramic. Figure 4a shows the bright field image of grain without obvious macrodomain contrast. Figure 4b displays the HRTEM image along the $[111]_{pc}$ (subscript pc stands for pseudocubic) zone axis. The corresponding FFT pattern is shown in Fig. 4c, which contains the fundamental reflection spots along with weak superstructure reflection spots 1/2(*ooe*), 1/2(*oeo*), and 1/2(*eoo*) (''*o*'' and ''*e*'' refer to odd and even *hkl* Miller indices, respectively) marked by cyan, red, and yellow circles, respectively. Herein, the above three distinctive reflection spots can be regarded as the three corresponding variants of $a^0a^0c^+$ in-phase oxygen octahedral tiltings with *P4bm* space group in BNT-based materials [15, 38]. To visualize the structural details, the HRTEM image was Fourier filtered and reconstructed using the three diffraction spots mentioned above. In the reconstructed image (see Fig. 4d), it is intuitive to discover that each variant is constituted by nanoscale regions and has a
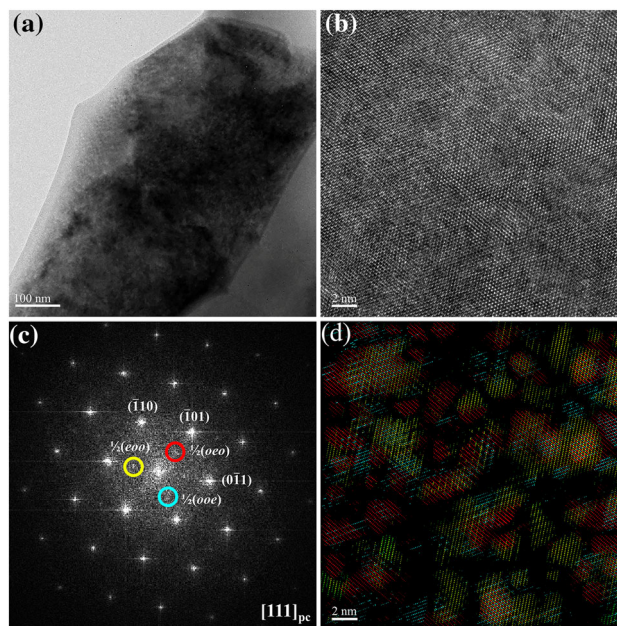

Fig. 4 **a** The bright field image of a grain in 0.75BNT-0.25BKT-0.03CZ. **b** The raw HRTEM image obtained from 0.75BNT-0.25BKT-0.03CZ along the $[111]_{pc}$ zone axis. **c** The corresponding FFT image of (**b**), in which yellow, cyan, and red circles mark the 1/2(*eoo*), 1/2(*ooe*), and 1/2(*oeo*) superstructure reflection spots, respectively. **d** This image was a superposition of three images created by filtering the original image using the spots mentioned above, respectively.

randomly scattered distribution. The above structural features further confirm the existence of PNRs [38].

Figure 5a–h depicts the polarization–electric field (*P–E*) hysteresis loops and current–electric field (*I–E*) curves of 0.75BNT-0.25BKT-*x*CZ samples obtained by applying an electric field of 70 kV/cm with a frequency of 1 Hz at RT. Without CZ doping, 0.75BNT-0.25BKT exhibits a saturated slanted rectangular hysteresis loop with apparent ferroelectric characteristics accompanied by a large spontaneous polarization P_s of 44.3 μC/cm^2, remnant polarization P_r of 32.9 μC/cm^2, and coercive field E_c of 27.0 kV/cm, respectively (see Fig. 5a). Correspondingly, two apparent current peaks (E_{F1} and E_{F2}) correlating to the coercive field in *I–E* curves can be observed in Fig. 5e, which can be attributed to the domain switching of long-range ferroelectric order [8, 15]. As the CZ content increases, the *P–E* loops become slender (see Fig. 5b–d) with a continuous reduction in P_s, P_r, and E_c to exhibit a relaxor characteristic (see Fig. S2). It is mostly due to the CZ incorporation disrupting the long-range ferroelectric order and enhancing the relaxation. Interestingly, the *P–E* loop

Fig. 5 P–E hysteresis loops and corresponding I–E curves of 0.75BNT-0.25BKT-xCZ samples, respectively, **a** and **e**: $x = 0$; **b** and **f**: $x = 0.01$; **c** and **g**: $x = 0.03$; and **d** and **h**: $x = 0.05$
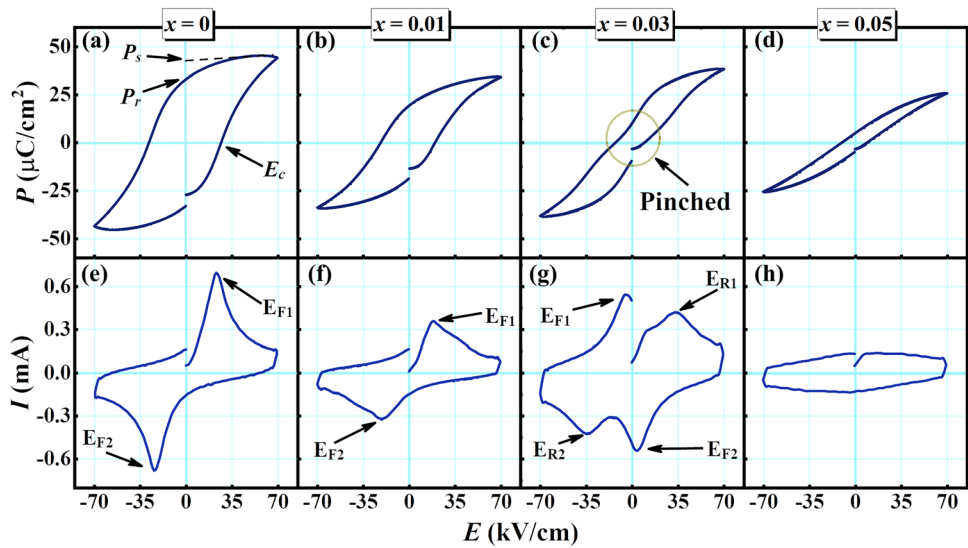
exhibits a distinct pinched feature for $x = 0.03$ with P_s of 35.31 $\mu C/cm^2$ even a small increase compared to $x = 0.01$, which can be interpreted as an electric field-induced non-polar to polar phase transition process and the dual contribution of ferroelectric and ergodic relaxor phases. Once applying the electric field, the PNRs considered non-polar phases due to their high dynamic before applying the electric field would respond to the external electric field and could be induced into a polarization state, resulting in an obvious pinched hysteresis loop [11, 39]. Subsequently, four current peaks rather than two peaks are observed in the I–E curve for $x = 0.03$, among which the peaks of E_{R1} and E_{R2} are generally ascribed to the phase transition from the ergodic relaxor state to the long-range ordered ferroelectric state [4, 31]. As x further increases to 0.05, the P–E loop becomes apparently slim with significantly reduced P_s and P_r. However, the E_c value remains basically unchanged compared to $x = 0.03$, which probably means that the long-range ferroelectric order has been entirely disrupted, resulting in an overwhelming amount of ergodic relaxor phase. And the current peaks broaden and flatten, along with the curve transforming into a rectangular-like shape, illustrating that the relaxor phase dominates and further confirming the formation of the "weakly coupled relaxor," in which the phase transition is difficult to induce even with a large electric field.

The bipolar strain hysteresis loops (bipolar S–E curves) with various x for 0.75BNT-0.25BKT-xCZ samples shown in Fig. 6a were obtained at RT under the electric field of 30 kV/cm, 50 kV/cm, and 70 kV/cm, respectively. For $x = 0$, the 0.75BNT-0.25BKT ceramic exhibits a butterfly-shaped curve indicating the typical ferroelectric feature [10]. As x increases, the bipolar strain hysteresis loops gradually transform into sprout-shaped curves, which implies the weakening of ferroelectricity and the enhancement of relaxation due to the disruption of long-range ferroelectric order and the generation of the ergodic relaxor phase with the CZ substitution increasing [15, 34]. In addition, the symmetry improvement of the bipolar strain hysteresis loops also suggests that the domain switching becomes easier with the increase of PNRs activity verified from the decreased variation of T_f estimated by the Vogel–Fulcher fitting [40, 41]. On the other hand, a negative strain (S_{neg}) and a positive strain (S_{pos}) (the inset in Fig. 6b) can be extracted from the bipolar strain hysteresis loops to further understand the electric field-induced strain behavior. A substantial S_{neg} for $x = 0$ manifests the apparent ferroelectricity under the electric field and S_{neg} along with S_{pos} significantly increases with the increasing electric field, while the symmetry of the bipolar strain hysteresis loops decreases [8]. Figure 6b shows the effects of CZ content on the variation of S_{neg} and S_{pos}. With increasing CZ content, S_{neg} and S_{pos} basically exhibit a downward trend. However, there was an exceptional increase of S_{pos} for $x = 0.03$ compared to $x = 0.01$, which should be ascribed to the reversible phase transition from the relaxor phase to the ferroelectric phase. Subsequently, S_{pos} for $x = 0.05$ decreases significantly and
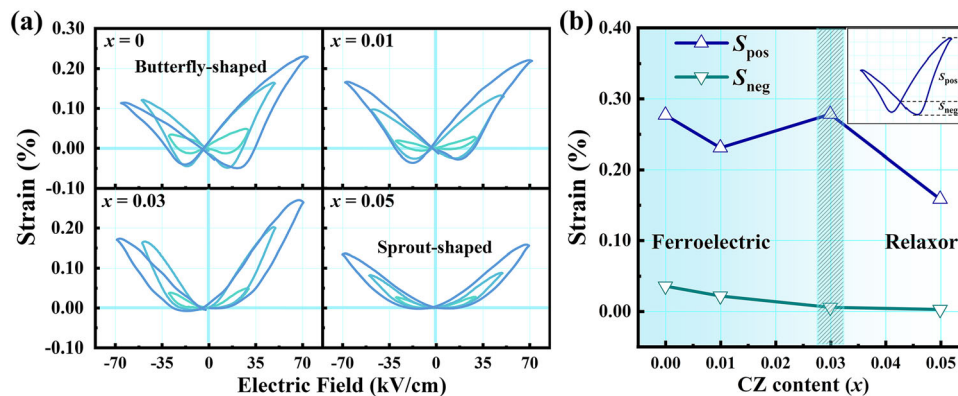
Fig. 6 **a** Bipolar strain hysteresis loops with various x under the electric field of 30 kV/cm, 50 kV/cm, and 70 kV/cm, respectively, at RT. **b** Positive strain (S_{pos}) and negative strain (S_{neg}) evolution as a function of x. The inset shows the estimation of S_{pos} and S_{neg}, which are the difference between the maximum strain and the strain at zero electric field and the difference between the minimum strain and the strain at zero electric field during bipolar cycles, respectively

S_{neg} decreases to approach zero due to the ergodic relaxor phase dominating. Actually, the variation trend of S_{pos} and S_{neg} is similar to that of P_s and P_r, which is also consistent with the dielectric temperature spectra, reflecting the process of composition-induced phase transition.

To evaluate the feasibility of practical applications, the unipolar electrostrain behaviors of 0.75BNT-0.25BKT-xCZ piezoelectric ceramics are investigated at RT. In Fig. 7a, the electric field-induced unipolar strain increases with increasing CZ content, reaching a maximum of 0.34% at $x = 0.03$ and then decreases with further increasing CZ content. The variation of the unipolar strain S_{max} under the electric field of 70 kV/cm is shown in Fig. 7b, where the variation of the piezoelectric coefficient (d_{33}) is also plotted. d_{33} decreases monotonously owing to the destruction of long-range ferroelectric order and the generation of the ergodic relaxor phase with increasing CZ content [28]. Interestingly, the unipolar strain S_{max} is the largest at $x = 0.03$, while d_{33} value of 65 pC/N is relatively small. The disparity between strain and d_{33} implies that the behavior of large electrostrain is no longer strongly connected to the piezoelectric response and the electrostrain mechanism should be changed. Based on the previous analysis, the ferroelectric and ergodic relaxor phases coexist at $x = 0.03$. Thus, it can be inferred that the strain is mainly driven by the electric field-induced reversible phase transition from the relaxor phase to the ferroelectric phase. Furthermore, hysteresis is another important parameter to evaluate the electrostrain behavior, which is deduced from the S–E curve (the inset

shown in Fig. 7b) [42]. Generally speaking, hysteresis is affected by domain switching closely related to the phase constitution and the electrostrain mechanism [1, 2]. With the increase of x, the ferroelectric phase decreases, while the relaxor phase increases, making the high dynamic PNRs in the ergodic relaxor state improve the response under the electric field. On the other hand, the electric field-induced phase transition, which usually needs to overcome the nucleation energy barrier, will lead to the unavoidable delay of strain response to some extent and thus increase the hysteresis [4, 9]. The final variation of hysteresis depends on the competing results of the above reasons. It is found that the hysteresis basically presents a downward trend with increasing x, but there is a moderate increase at $x = 0.03$, which is mainly attributed to the coexistence of ferroelectric and relaxor phases here and a significant relaxor ferroelectric phase transition under the applied electric field.

The above analysis of electrostrain behavior with varying compositions shows that the composition of $x = 0.03$ has excellent comprehensive performance. Then, the electrostrain behavior of this composition under different electric fields is further explored to better understand the origin of the large strain. Figure 7c depicts the unipolar strain under various electric fields. It can be observed that the strain value increases substantially over 20 kV/cm. Then, the increase rate slows down and it basically keeps a linear increase with applying the electric field above 40 kV/cm. Correspondingly, the maximum value of strain S_{max} and the normalized strain (S_{max}/E_{max})

Fig. 7 **a** Unipolar strain loops with different x. **b** Strain, hysteresis, and d_{33} as a function of x. **c** Unipolar S–E curves of 0.97 (0.75BNT-0.25BKT)-0.03CZ with electric fields ranging from 20 to 70 kV/cm at RT. **d** The corresponding maximum strain and normalized strain (S_{max}/E_{max}) at various electric fields
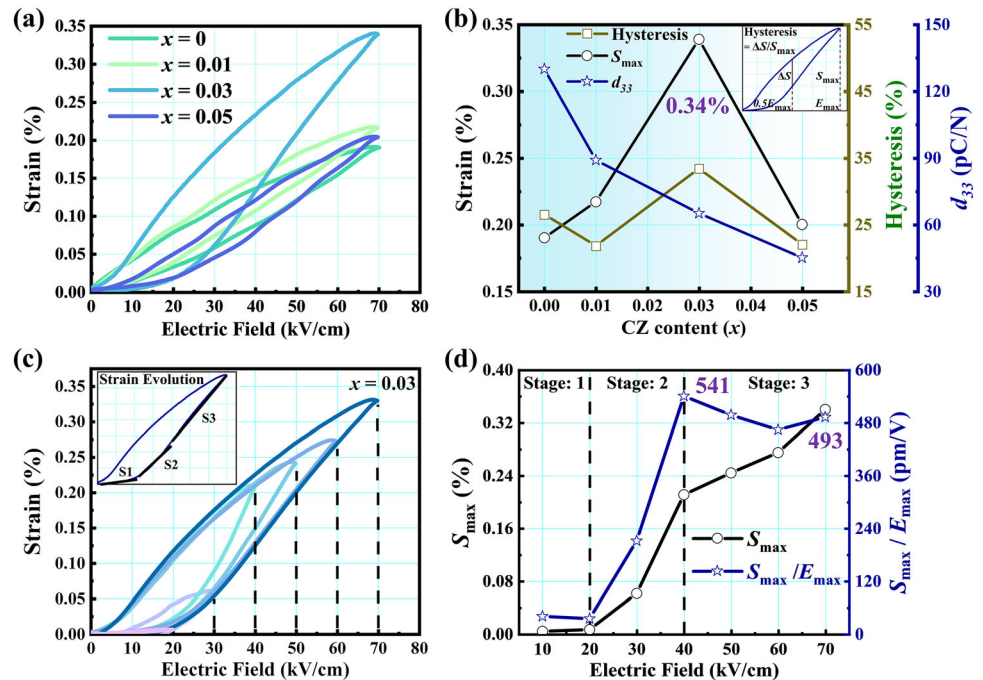
under various electric fields are illustrated in Fig. 7d. According to the evolution of unipolar strain under various electric fields, three stages of strain increase could be deduced. In the first stage, with the applying electric field of no more than 20 kV/cm, the normalized strain value is almost negligible with S_{max} only about 0.006% at 20 kV/cm exhibiting a small sprout-shaped curve. It is judged that the increased strain could be triggered by the electrostriction effect at a low electric field [15]. As the electric field gradually increases from 20 to 40 kV/cm, the strain value increases tremendously by 35 times until 0.21% at 40 kV/cm with a maximum value of normalized strain (541 pm/V). The rapid increase in this stage should be mainly attributed to the relaxor to ferroelectric phase transition driven by the applying electric field [10]. Subsequently, at the final stage as the electric field further increases over 40 kV/cm, the increase of strain value tends to slow down, showing an almost linear relationship with the increase of electric field, which indicates that the increase of strain at this stage could be dominantly ascribed to the piezoelectric response [29].

Figure 8 depicts the comparison of strain and hysteresis in BNT-based ceramics between the previously reported and this work. The detailed information is recorded in Table. S1. It can be seen that the large strain generally has large hysteresis, whereas the small hysteresis usually accompanies with small

strain. In fact, it is ideal to achieve both large strain and low hysteresis simultaneously (i.e., the direction indicated by the curved up arrow in Fig. 8). However, increasing strain is often at the expense of increasing hysteresis and vice versa [1, 4]. Therefore, how to balance the two sides through reasonable design to obtain excellent comprehensive performance is an important topic for practical application. Here, through the composition design strategy using the method of slightly deviating from the MPB base composition and introducing a suitable CZ content, a large strain of 0.34% and a relatively small hysteresis of 33.4% were obtained in the 0.97(0.75BNT-0.25BKT)-0.03CZ ceramics. Compared with the counterpart 0.78BNT-0.22BKT-xCZ with MPB base composition, the hysteresis in this work is reduced dramatically by about 40%, while the strain is remained essentially unaltered, which can be applied to high-sensitivity actuators.

4 Conclusion

In summary, 0.75BNT-0.25BKT-xCZ (x = 0, 0.01, 0.03, 0.05) ceramics were successfully synthesized by the solid-state reaction method. All the samples have a pure perovskite structure with dense surface morphology. The X-ray diffraction patterns and dielectric temperature spectra reveal that the phase structure

Fig. 8 Strain and hysteresis of previously reported BNT-based ceramics compared with this work
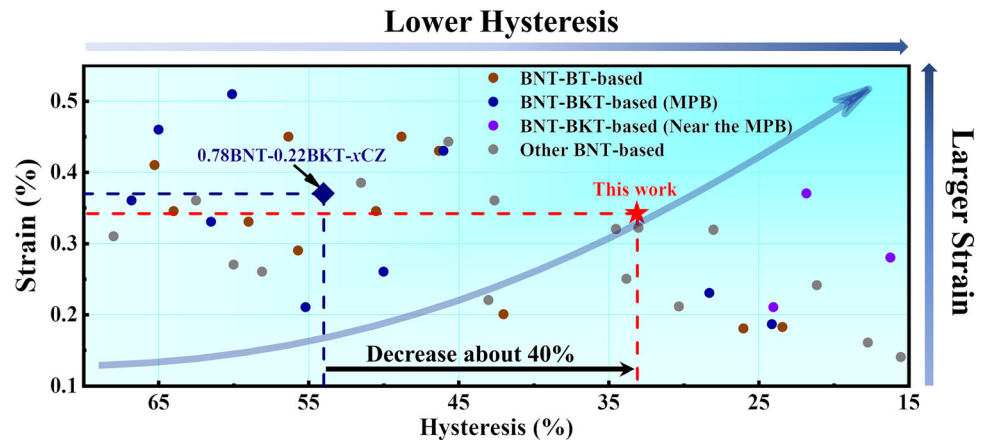
gradually transforms into the pseudocubic phase. The coexistence of ferroelectric and relaxor phases with the formation of the weakly coupled relaxor enhances relaxation, which is associated with the existence of high dynamic PNRs confirmed by the HRTEM imaging. Further, it is demonstrated through the slender P–E hysteresis loops and flattening in I–E curves. The pinched P–E hysteresis loop with four current peaks in the I–E curve was unambiguously observed at $x = 0.03$, which indicates the coexistence of ferroelectric and relaxor phases. Consequently, a large strain up to 0.34% with a normalized strain of about 500 pm/V is acquired for $x = 0.03$, which should be contributed by the reversible phase transition from the relaxor phase to the ferroelectric phase. On the other hand, in contrast to the counterpart system that generally has a large hysteresis of over 50%, the relatively low hysteresis of about 33% is successfully obtained due to the high dynamic PNRs in the ergodic relaxor state that improves the response under the electric field. The tradeoff between the large strain and low hysteresis is realized by the composition design strategy using the method of slight deviation of the MPB base composition and introducing a suitable component, which is promising for high-sensitivity actuators and paving a way for designing lead-free electrostrain ceramics with excellent comprehensive performance in the future.

Author contributions

All authors contributed to the study conception and design. Material preparation, data collection, and analysis were performed by HZ, JW, FH, TN, JL, YW, HX, MM, JH, BL, and KS. The first draft of the manuscript was written by HZ and MM, and all authors commented on previous versions of the manuscript. All authors read and approved the final manuscript.

Data availability

The data that support the findings of this study are available from College of Electronics and Information, Hangzhou Dianzi University, but restrictions apply to the availability of these data, which were used under license for the current study and so are not publicly available. Data are, however, available from the authors upon reasonable request and with permission of Prof. Dr. Minmin Mao.

Declarations

Conflict of interest The authors declare that they have no known competing financial interests or personal relationships that could have appeared to influence the work reported in this paper.

References

1. P. Fan, K. Liu, W. Ma, H. Tan, Q. Zhang, L. Zhang, C. Zhou, D. Salamon, S.-T. Zhang, Y. Zhang, B. Nan, H. Zhang, J. Materiomics **7**, 508–544 (2021)

2. J. Hao, W. Li, J. Zhai, H. Chen, Mat. Sci. Eng. R **135**, 1–57 (2019)

3. X. Zhou, G. Xue, H. Luo, C.R. Bowen, D. Zhang, Prog Mater. Sci. **122**, 100836 (2021)

4. Z. Liu, T. Ruan, Q. Li, Y. Liu, Y. Lyu, M. Mao, Mater. Res. Express **8**, 056303 (2021)

5. L. Jin, W. Luo, L. Hou, Y. Tian, Q. Hu, L. Wang, L. Zhang, X. Lu, H. Du, X. Wei, Y. Yan, G. Liu, J. Eur. Ceram. Soc. **39**, 295–304 (2019)

6. L. Jin, J. Pang, R. Jing, Y. Lan, L. Wang, F. Li, Q. Hu, H. Du, D. Guo, X. Wei, Z. Xu, L. Zhang, G. Liu, J. Alloys Compd. **788**, 1182–1192 (2019)

7. K. Wang, A. Hussain, W. Jo, J. Rödel, D.D. Viehland, J. Am. Ceram. Soc. **95**, 2241–2247 (2012)

8. J. Wu, H. Zhang, C.-H. Huang, C.-W. Tseng, N. Meng, V. Koval, Y.-C. Chou, Z. Zhang, H. Yan, Nano Energy **76**, 105037 (2020)

9. L. Wu, S. Zhang, J. Liu, Q. Hu, J. Chen, Y. Wang, B. Xu, Y. Xia, J. Yin, Z. Liu, Ceram. Int. **42**, 13783–13789 (2016)

10. T. Li, X. Lou, X. Ke, S. Cheng, S. Mi, X. Wang, J. Shi, X. Liu, G. Dong, H. Fan, Y. Wang, X. Tan, Acta Mater. **128**, 337–344 (2017)

11. Y. Yang, R. Jing, J. Wang, X. Lu, H. Du, L. Jin, Ceram. Int. **48**, 23975–23982 (2022)

12. S.-T. Zhang, A.B. Kounga, E. Aulbach, H. Ehrenberg, J. Rödel, Appl. Phys. Lett. **91**, 112906 (2007)

13. J. Hao, B. Shen, J. Zhai, H. Chen, J. Appl. Phys. **115**, 034101 (2014)

14. X. Liu, F. Li, P. Li, J. Zhai, B. Shen, B. Liu, J. Eur. Ceram. Soc. **37**, 4585–4595 (2017)

15. H. Xi, L. Yu, H. Qian, F. Chen, M. Mao, Y. Liu, Y. Lyu, J. Mater. Sci. **55**, 1388–1398 (2019)

16. H. Qian, Z. Yu, M. Mao, Y. Liu, Y. Lyu, J. Eur. Ceram. Soc. **37**, 3483–3491 (2017)

17. J. Han, J. Yin, J. Wu, J. Am. Ceram. Soc. **103**, 412–422 (2019)

18. G. Dong, H. Fan, L. Liu, P. Ren, Z. Cheng, S. Zhang, J. Materiomics **7**, 593–602 (2021)

19. X. Zhou, H. Qi, Z. Yan, G. Xue, H. Luo, D. Zhang, ACS Appl. Mater. Inter. **11**, 43107–43115 (2019)

20. S.K. Rout, V. Chauhan, D.K. Kushvaha, E. Sinha, A. Hussain, B. Tiwari, J. Mater. Sci. Mater. Electron. **29**, 19524–19531 (2018)

21. L. Zhang, S. Cao, Y. Li, R. Jing, Q. Hu, Y. Tian, R. Gu, J. Kang, D.O. Alikin, V.Y. Shur, X. Wei, G. Liu, F. Gao, H. Du, Y. Yan, L. Jin, J. Alloys Compd. **896**, 163139 (2022)

22. H. Pan, J. Zhang, X. Jia, H. Xing, J. He, J. Wang, F. Wen, Ceram. Int. **44**, 5785–5789 (2018)

23. U. Obilor, C. Pascual-Gonzalez, S. Murakami, I.M. Reaney, A. Feteira, Mater. Res. Bull. **97**, 385–392 (2018)

24. C.C. Jin, F.F. Wang, L.L. Wei, J. Tang, Y. Li, Q.R. Yao, C.Y. Tian, W.Z. Shi, J. Alloys Compd. **585**, 185–191 (2014)

25. H. Xie, L. Yang, S. Pang, C. Yuan, G. Chen, H. Wang, C. Zhou, J. Xu, J. Phys. Chem. Solids **126**, 287–293 (2019)

26. H. Wang, Q. Li, Y. Jia, A.K. Yadav, B. Yan, M. Li, Q. Shen, Q. Quan, W. Wang, G. Dong, H. Fan, J. Alloys Compd. **879**, 160378 (2021)

27. X. Ren, H. Yin, Y. Tang, H. Fan, H. Yuan, Ceram. Int. **46**, 1876–1882 (2020)

28. Y. Yang, J. Xu, L. Yang, C. Zhou, H. Zhang, G. Zhang, H. Wang, G. Rao, Z. Huo, X. Liu, H. Wu, Mater. Chem. and Phys. **276**, 125402 (2022)

29. P. Shi, T. Li, X. Lou, X. Zu, X. Zhu, C. Zhou, Q. Liu, L. He, X. Zhang, S. Yang, J. Alloys Compd. **860**, 158369 (2021)

30. M. Wang, Q. Feng, Y. Wei, N. Luo, C. Yuan, C. Zhou, T. Fujita, J. Xu, G. Chen, J. Phys. Chem. Solids **157**, 110209 (2021)

31. K. Han, N. Luo, Z. Chen, L. Ma, X. Chen, Q. Feng, C. Hu, H. Zhou, Y. Wei, F. Toyohisa, J. Eur. Ceram. Soc. **40**, 3562–3568 (2020)

32. R. Li, C. Zhou, L. Hou, C. Yuan, J. Xu, Q. Li, S. Cheng, G. Rao, J. Mater. Sci. Mater. Electron. **33**, 6121–6130 (2022)

33. Y. Wan, L. Tang, X. Dang, P. Ren, M. Ma, K. Song, G. Zhao, Ceram. Int. **45**, 2596–2601 (2019)

34. X. Wang, X. Wu, D. Yang, J. Yin, J. Wu, Chem. Eng. J. **447**, 137494 (2022)

35. F. Yang, Y. Chen, X. Li, W. Huang, G. Wang, X. Dong, Ceram. Int. **47**, 25785 (2021)

36. J. Wu, A. Mahajan, L. Riekehr, H. Zhang, B. Yang, N. Meng, Z. Zhang, H. Yan, Nano Energy **50**, 723 (2018)

37. P. Zhao, Z. Fang, X. Zhang, J. Chen, Y. Shen, X. Zhang, Q. An, C. Yang, X. Gao, S. Zhang, B. Tang, ACS Appl. Mater. Inter. **13**, 24833 (2021)

38. I. Levin, I.M. Reaney, Adv. Funct. Mater. **22**, 3445 (2012)

39. Y. Yang, R. Jing, J. Wang, L. Zhang, Y. Huang, L. Jin, Ceram. Int. **48**, 14329–14337 (2022)

40. T. Meng, Q. Li, C. Zhou, W. Li, S. Cheng, C. Yuan, J. Xu, G. Rao, J. Mater. Sci. Mater. Electron. **33**, 6802–6815 (2022)

41. D. Viehland, S.J. Jang, L.E. Cross, M. Wuttig, Phys. Rev. B **46**, 8003–8006 (1992)

42. A. Deng, J. Wu, J. Eur. Ceram. Soc. **41**, 5147–5154 (2021)